Article

MMS

Mathematics and Mechanics of Solids
2022, Vol. 27(10) 2314–2337
© The Author(s) 2022
Article reuse guidelines:
sagepub.com/journals-permissions
DOI: 10.1177/10812865221114299
journals.sagepub.com/home/mms
SAGE

Experimental and numerical investigation of the deformation behaviour of cables and thin beam-like structures under multi-axial loading

André Hildebrandt
Hamburg University of Technology, Germany

Prateek Sharma
Saarland University, Germany

Alexander Düster
Hamburg University of Technology, Germany

Stefan Diebels
Saarland University, Germany

Received 31 January 2022; accepted 27 June 2022

Abstract
In various applications, it is common to use thin beam-like structures, made of plastic or fibre-reinforced materials, as well as components such as cables. They are flexible, and the most common form of deformation is bending, but they can also be stretched or torqued. Due to their structural composition, a coupling between the different loading directions exists. This is especially pronounced for cables, where the different components interact with each other and the kinematics of each component are different. Thus, to characterise these materials, it is necessary to consider tension, torsion, bending, and a coupling of the three load cases. In this work, such characterisations are performed for a polyvinyl chloride rod, a carbon fibre-reinforced rod, and a coaxial cable. The three materials represent the isotropic and anisotropic material classes and include homogeneous and non-homogeneous cross-sections. An anisotropic elasto-plastic material model is implemented in the finite element method to model the behaviour of such structures. The material model includes anisotropic plasticity so that the structural effects can also be modelled for large deformations. Thin structures are discretised with higher-order elements, and a comparison of the experimental and the simulation results is presented.

Keywords
Cables, beams-like structures, anisotropy, anisotropic plasticity, coupled loading

Corresponding author:
Prateek Sharma, Applied Mechanics, Saarland University, Campus A4.2, 66123 Saarbrücken, Saarland, Germany.
Email: prateek.sharma@uni-saarland.de

1. Introduction

With increasing digitalisation, the growth of electro-mobility, and the extensive use of robots in industry 4.0, the use of cables has increased. In real-world applications, thin flexible structures such as cables can undergo tensile, torsional, or bending deformation. Their behaviour is characterised by the different stiffnesses for different load cases—either due to geometrical effects or due to their structural composition [1–3]. It is important to characterise these structures for all three load cases as the stiffness in one direction is not enough to model the behaviour accurately [1,4–6]. The tensile stiffness $(EA)_s$, the torsional stiffness $(GJ)_t$, and the bending stiffness $(EI)_b$ can be directly determined from experiments such as tensile tests, torsion tests, or bending tests. However, there are many examples in the literature that there are interactions between the different deformation modes—and that the stiffness in one direction influences the deformation in another direction [1,3,7,8]. These couplings between the stiffnesses are mostly due to structural effects such as the orientation of the fibres in a fibre-reinforced material or due to interaction between the wires in a cable. To study these interactions, apart from the classical experiments, multi-axial experiments need to be conducted, where loading is simultaneously applied in two different directions.

The modelling of thin structures includes the consideration of the anisotropic behaviour of the material, on one hand, and the discretisation of the macroscopic geometry, on the other hand. Higher-order elements serve as a basis to model the thin but long structures with finite element method (FEM). The discretisation must be able to represent large deformations but should not be computationally expensive. Plastic deformation should be included as well—coupled with the anisotropy, so that the structural effects of the different components in a fibre-reinforced material or a cable can be taken into account.

In this work, apart from the classical tensile, torsional, and three-point bending tests, free bending and free bending coupled with torsion tests were performed on the three different types of material, namely, polyvinyl chloride (PVC), carbon fibre–reinforced plastic (CFRP), and a coaxial cable. While PVC is isotropic, CFRP represents the class of material that is anisotropic but has a homogeneous cross-section on the macro scale, while the coaxial cable represents the anisotropic case with an inhomogeneous cross-section resulting from the internal structure of the cable. In CFRP, the interaction between the components is minimal compared to the interaction between the components of a coaxial cable. In order to model the behaviour of the different materials, an elasto-plastic material model is implemented in non-linear FEM with the help of higher-order elements. The experimental results are compared with the numerical solution to determine the parameters for the model. The simulations are validated using an experiment in another loading direction. Thus, a numerical model that can reproduce the anisotropic behaviour of thin flexible structures is presented.

2. Experimental methods

Five different types of experiments were carried out to characterise the material under different load cases. A brief explanation of the methods used to conduct these experiments is provided. In general, the rate-dependent effects were not considered in the material model, and hence, all tests were conducted at the same strain rate.

2.1. Uniaxial tensile tests

The uniaxial tensile tests were carried out by applying a displacement-driven load in the axial direction of the cylindrical flexible structures. The samples were fixed at both ends using pneumatic clamps to ensure a constant contact pressure of 0.3 MPa between the test samples and the clamps. One end of the sample was fixed, while the other end was driven with a motor to apply the axial displacement (Figure 1(a)). Axial displacement-controlled loading was applied at a given rate up to the maximum displacement, followed by an unloading cycle until the applied load was zero. The reaction force during the loading and unloading cycle was continuously recorded using a sensor at the fixed end of the sample. The uniaxial tensile test was conducted on a commercial universal testing machine. The displacement applied to the sample was recorded by the encoders of the universal testing machine. In addition, the strain in the sample was measured using three high-speed cameras that monitored the distortion of a speckle pattern painted on the surface of the sample using the digital image correlation (DIC) method

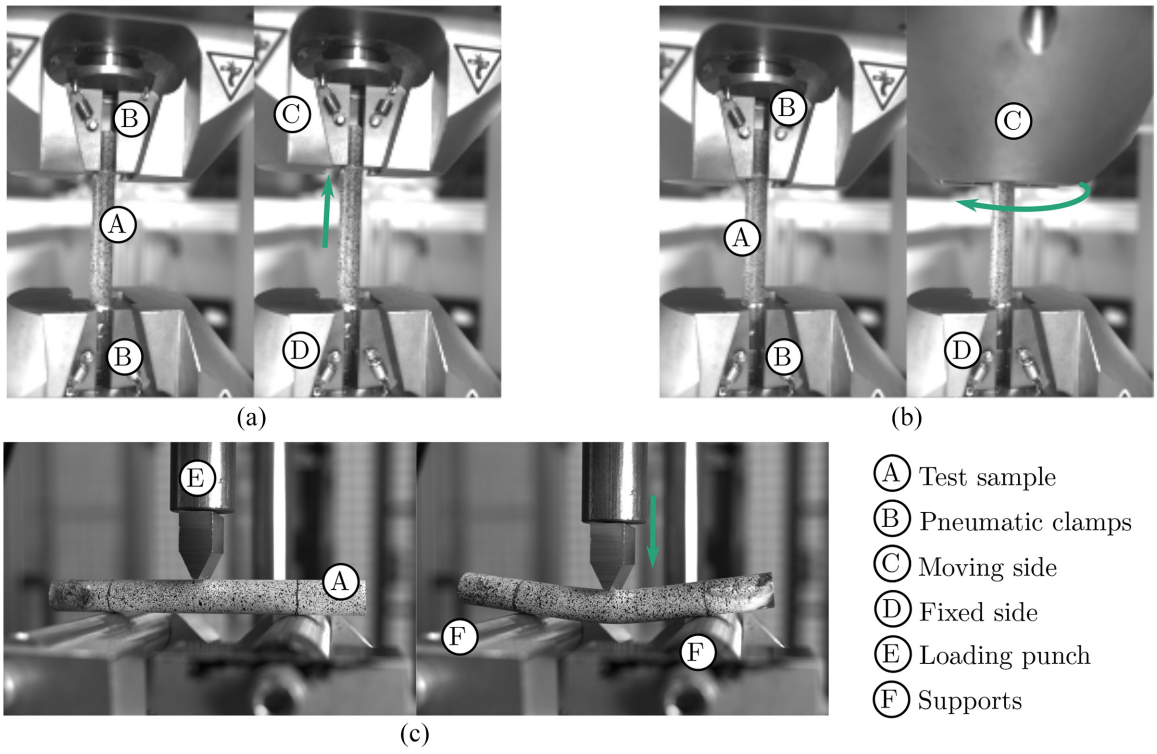

Figure 1. The three basic experiments conducted for the thin flexible structures: (a) uniaxial tensile test, (b) torsion test, and (c) three-point bending test.

[9]. In this method, a black and white pattern is sprayed onto the surface of the sample. Then, images are recorded at regular time intervals with the help of calibrated high-speed cameras. Any change in the pattern can later be correlated to displacements using the DIC software. A commercial software was used for the calibration of the cameras and the evaluation of the images.

2.2. Torsion tests

Similar to the uniaxial tensile test, pneumatic clamps were used to hold the ends of the sample. However, in contrast to the tensile load, a rotation was applied at one end of the sample while the other end was fixed (Figure 1(b)). The distance between the two ends was kept constant during the torsion test. The torsional moment was recorded continuously with the help of the internal sensor, and the applied rotation was recorded by the encoders in the drive of the machine. Similar to the tensile tests, a DIC was carried out as well using images from three high-speed cameras to record the three-dimensional (3D) deformation on the surface of the samples.

2.3. Three-point bending tests

In order to conduct the three-point bending tests, the samples were placed horizontally on two cylindrical supports with radius r_s. Using a motor-driven circular punch of radius r_p, a deflection was applied to the sample exactly in between the two supports (Figure 1(c)). The distance between the two supports was adjusted to a given value L_x. The tests were carried out on the *three-point bending* test stand (Figure 1(c)). If deflection $\bar{u}_y$ is applied, this results in the bending strain:

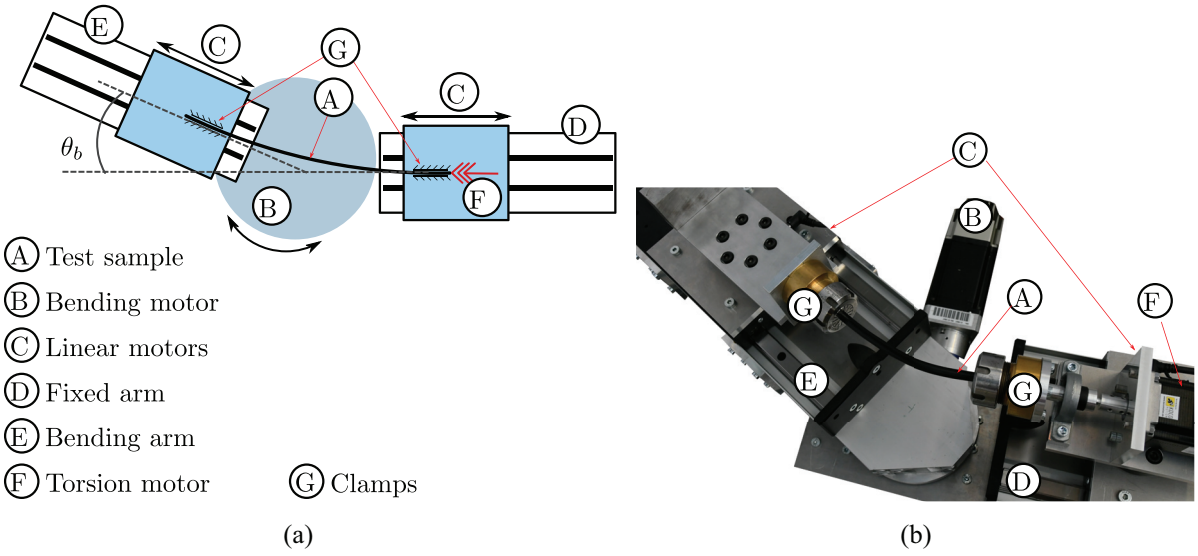

Figure 2. Top view for the free bending test setup: (a) schematic diagram of the free bending test setup and (b) test setup.

$$\varepsilon_b = \frac{12\bar{u}_y r_n}{L_x^2}. \tag{1}$$

Here, r_n denotes the distance from the neutral axis at which the strain is calculated. In the experiment, the maximum strain occurred at the edges of the bending sample, and the strain rate at the outer edge was matched to the strain rate in the tensile and torsion test. The reaction force on the loading punch was measured continuously with the help of a force sensor mounted along the axis of the punch. The deflection of the sample was measured with the help of the encoders on the motor driving the loading punch. Generally, the three-point bending test is suitable for small deflections, while larger deflections tend to cause local deformations in the samples because of the high stress concentrations at the contact points. In addition, the sample may slip at the contact points, which leads to a distorted and erroneous bending deformation.

2.4. Free bending tests

Apart from the three-point bending test, samples were also tested under free bending with the help of a self-developed test setup. In the setup, a bending motion was applied directly to the sample, allowing for larger deformations than in three-point bending tests. One end of the sample is clamped to a fixed arm, whereas the other end was mounted on a movable arm. The movable arm served to create a circular motion around the centre of the sample, resulting in bending of the sample. In this way, a bending moment perpendicular to the plane of the circular motion was generated. The clamps for both ends of the sample were mounted on two separate linear motors. The circular motion generated an axial force in the sample, which is compensated by the motion of the linear motors along their current axis (Figure 2). Thus, both ends were free to move along their axis—resulting in a pure bending deformation. The forces and the moments on the samples were recorded with the help of two 6-axis-sensors mounted on both ends of the sample. The sensor mounted on the movable arm was named S89, and the sensor on the fixed arm was named S90. The circular motion of the movable arm was achieved with the help of a servo motor, and the resulting bending curvature was recorded with the help of this motor's position. The rate of bending was kept low enough to allow for a compensation of the axial force by the linear motors. It can be seen that the curvature given by:

$$K_b = \frac{1}{R} = \frac{\theta_b}{L_x}, \tag{2}$$

changes at the same rate as the strain rate for the other experiments. Here, R denotes the radius of the arc formed by the test sample, θ_b is the bending angle, and L_x is the length of the cable sample.

2.5. Free bending with torsion tests

In order to test the samples under coupled loading conditions, the samples were torqued and bent simultaneously. In the free bending test setup, the clamp on one end of the sample was connected to an additional servo motor that served to rotate the sample around its axis, resulting in a superimposed torsional motion. During the coupled tests, the samples were first rotated until a given torsional degree was achieved. In the second phase, the bending motion was applied.

3. Numerical methods

In order to compute the deformation of the slender structures, the non-linear FEM is used. Specifically, the *p*-FEM combined with hierarchic shape functions and quasi-regional mapping is applied as it offers high accuracy of geometrical representations and a fast convergence with relatively few elements and degrees of freedom [10,11]. In addition to the high convergence rates, the *p*-FEM is less prone to locking effects. The hexahedral solid element formulation is a pure displacement-based formulation (no rotational degrees of freedom are required) that includes a full 3D strain and stress state, which makes it relatively easy to implement even complex material models. The slender structure of the rods and cables can be taken into account by anisotropic ansatz spaces using different polynomial degrees for the shape functions in different local directions.

To keep the computational effort low, the internal structure of the cables is not resolved. A homogeneous material is used along the cross-section instead. Consequentially, the material model used describes effective material properties on the macro scale. Therefore, it is chosen to be anisotropic in the hyperelastic and elasto-plastic regime. Due to the anisotropy, it is possible to capture non-linear effects such as friction between parts or reordering of the parts. An alternative approach that promises high efficiency with regards to the computational effort is the usage of one-dimensional Cosserat beams [12] or other beam elements that allow for an anisotropic behaviour [13,14]. The constitutive behaviour can be chosen such that an independent treatment of each of the load cases is possible, and thus offers the ability to easily represent them, when identifying the corresponding material properties. However, our aim is to avoid treating the rotations separately, and thus, we focus on high-order elements throughout this work. A short introduction regarding the kinematic and constitutive equations for the used material model is given in the following sections. This is followed by a description of the method used for the parameter identification (ID) and a short convergence study regarding the accuracy of the numerical simulations.

3.1. Kinematics

First, a body $\Omega \subset \mathbb{R}^3$ is defined in the initial configuration. It can also be described in the current configuration Ω_t at any time t by making use of the mapping $\varphi_t : \Omega \rightarrow \Omega_t$. A continuous description of each point is given by $\boldsymbol{X} \in \Omega$ in the initial configuration and $\boldsymbol{x} = \varphi_t(\boldsymbol{X}, t)$, $\boldsymbol{x} \in \Omega_t$ in the current configuration. Here, we apply the convention of using small letters for the current configuration and capital letters for its counterpart in the initial configuration. The deformation of the body can be described by the deformation gradient $\boldsymbol{F} = \nabla \varphi_t(\boldsymbol{X}, t)$. In order to incorporate inelastic deformations, it is multiplicatively decomposed:

$$\boldsymbol{F} = \boldsymbol{F}_\mathrm{e}\boldsymbol{F}_\mathrm{p}, \tag{3}$$

into elastic $\boldsymbol{F}_\mathrm{e}$ and volume preserving plastic $\boldsymbol{F}_\mathrm{p}$ parts [15–17]. The right Cauchy–Green tensor is defined as $\boldsymbol{C} = \boldsymbol{F}^\mathrm{T}\boldsymbol{F}$. Based on the multiplicative split in equation (3), an elastic and a plastic deformation measure can be defined as $\boldsymbol{C}_\mathrm{e} = \boldsymbol{F}_\mathrm{e}^\mathrm{T}\boldsymbol{F}_\mathrm{e}$ and $\boldsymbol{C}_\mathrm{p} = \boldsymbol{F}_\mathrm{p}^\mathrm{T}\boldsymbol{F}_\mathrm{p}$, respectively. The elastic part later serves as a basis for the description of the hyperelastic strain energy function. The time derivative of the deformation gradient $\dot{\boldsymbol{F}}$ is related to the spatial velocity gradient $\boldsymbol{l}$ in the current configuration or $\boldsymbol{L}$ in the reference configuration by:

$$\dot{\boldsymbol{F}} = \boldsymbol{l}\boldsymbol{F} = \boldsymbol{F}\boldsymbol{L}, \tag{4}$$

where $\boldsymbol{L}$ is a result of the pull back operation of $\boldsymbol{l}$ [18]. The velocity gradient in the reference configuration can also be divided into an inelastic and an elastic part, where the inelastic part [18] is defined by:

$$\boldsymbol{L}_{\mathrm{p}} = \boldsymbol{F}_{\mathrm{p}}{}^{-1}\dot{\boldsymbol{F}}_{\mathrm{p}}. \tag{5}$$

3.2. Constitutive equations: anisotropic finite strain elasto-plasticity

This section serves to provide a brief overview of the most important aspects of the anisotropic finite strain elasto-plasticity model, as proposed by Sansour et al. [18]. The dissipation inequality:

$$D = \boldsymbol{\Xi} : \boldsymbol{L} - \rho_0 \dot{\Psi}(\boldsymbol{C}_{\mathrm{e}}, Z) \geqslant 0, \tag{6}$$

forms the basis. It consists of the free energy function $\Psi(\boldsymbol{C}_{\mathrm{e}}, Z)$ and the internal power density $\boldsymbol{\Xi} : \boldsymbol{L} = \tau : \boldsymbol{l}$, with the Kirchhoff stress tensor τ and an Eshelby-like stress tensor $\boldsymbol{\Xi} = \boldsymbol{F}^{\mathrm{T}}\tau\boldsymbol{F}^{-\mathrm{T}}$. The free energy function is split additively into an elastic $\Psi_{\mathrm{e}}(\boldsymbol{C}_{\mathrm{e}})$ and an inelastic part $\Psi_{\mathrm{p}}(Z)$,

$$\Psi_{\mathrm{e}}(\boldsymbol{C}_{\mathrm{e}}, Z) = \Psi_{\mathrm{e}}(\boldsymbol{C}_{\mathrm{e}}) + \Psi_{\mathrm{p}}(Z), \tag{7}$$

where Z denotes an internal variable and corresponds to the accumulated plastic strain. In order to define an anisotropic behaviour, three structural tensors $\boldsymbol{M}_i$, $i = 1, 2, 3$ are introduced. They are defined by three orthonormal privileged directions $\boldsymbol{v}_i$, such that:

$$\boldsymbol{M}_i = \boldsymbol{v}_i \otimes \boldsymbol{v}_i. \tag{8}$$

The anisotropy of the elastic and inelastic parts can differ using a separate set of structural tensors for the elasticity and inelasticity. As this is not desirable in our case, no discrimination is made between the two sets. Using the elastic right Cauchy–Green tensor, a set of six invariants:

$$J_i = \mathrm{tr}(\boldsymbol{M}_i\boldsymbol{C}_{\mathrm{e}}),\ i = 1, 2, 3, \tag{9}$$

$$J_{i+3} = \mathrm{tr}(\boldsymbol{M}_i\boldsymbol{C}_{\mathrm{e}}^2),\ i = 1, 2, 3, \tag{10}$$

can be defined, where tr(·) denotes the trace of a tensor. Given those invariants, the quadratic elastic strain energy density function is defined as:

$$\Psi_{\mathrm{e}} = \sum_{i=1}^{3}\left[\alpha_i J_i + \frac{1}{2}\alpha_{i+3}J_i^2 + \alpha_{i+9}J_{i+3}\right] + \alpha_7 J_1 J_2 + \alpha_8 J_1 J_3 + \alpha_9 J_2 J_3. \tag{11}$$

The material parameters α_i, $i = 1, ..., 12$ are listed in Appendix 1 and are based on Sansour et al. [18].

Similarly to the elastic behaviour, the inelastic behaviour is described using six invariants based on the structural tensors $\boldsymbol{M}_i$ and (in this case) on the stress tensor $\boldsymbol{\Xi}$,

$$I_i = \mathrm{tr}(\boldsymbol{M}_i\mathrm{dev}(\boldsymbol{\Xi})),\ i = 1, 2, 3, \tag{12}$$

$$I_{i+3} = \mathrm{tr}(\boldsymbol{M}_i(\mathrm{dev}(\boldsymbol{\Xi}))^2),\ i = 1, 2, 3, \tag{13}$$

where $\mathrm{dev}(\boldsymbol{a}) = \boldsymbol{a} - \frac{\mathrm{tr}(\boldsymbol{a})}{3}\boldsymbol{1}$ denotes the deviatoric part of a second-order tensor $\boldsymbol{a}$. Herein, $\boldsymbol{1}$ is used for the unity tensor. These invariants can be combined with the material parameters β_i (see Appendix 1) to set up a suitable normalised equivalent stress:

$$\chi = \sum_{i=1}^{3}\left[\beta_i I_i^2 + \beta_{i+6}I_{i+3} + \frac{1}{2}\sum_{j=1}^{3}\beta_{i+j+1}I_i I_j\right], \quad i \neq j, \tag{14}$$

that reflects the anisotropic criterion for plastic flow within the yield function:

$$\phi = \sqrt{\frac{2}{3}}\left[\sigma_{11}^{\mathrm{y}}\sqrt{\chi} - (\sigma_{11}^{\mathrm{y}} - Y)\right], \tag{15}$$

where Y defines non-linear isotropic hardening:

$$Y = -\rho_0 \frac{\partial \Psi}{\partial Z} = -HZ - (\sigma_\infty - \sigma_{11}^{\mathrm{y}})(1 - e^{-\eta Z}). \tag{16}$$

Herein, further material parameters are introduced: σ_∞ is the saturation stress, H is the linear hardening parameter, η is the exponential hardening parameter, and σ_{11}^{y} is the yield stress in direction of $\boldsymbol{v}_1$. The principle of maximum dissipation defines the plastic flow based on the variational form:

$$\int \left(\lambda \phi(\boldsymbol{\Xi}, Y) - (\boldsymbol{\Xi} : \boldsymbol{L}_{\mathrm{p}} + Y\dot{Z})\right) \mathrm{d}s = \text{stationary}, \tag{17}$$

where λ is the plastic multiplier and $\mathrm{d}s$ refers to the deformation path. The variation yields the associated evolution equations for the hardening parameter:

$$\dot{Z} = \lambda \frac{\partial \phi}{\partial Y}, \tag{18}$$

and the flow rule:

$$\boldsymbol{L}_{\mathrm{p}} = \lambda \frac{\partial \phi}{\partial \boldsymbol{\Xi}}. \tag{19}$$

Loading and unloading conditions are defined in the Kuhn–Tucker form,

$$\phi \leqslant 0, \quad \dot{\lambda} \geqslant 0, \quad \dot{\lambda}\phi = 0. \tag{20}$$

Finally, the time integration of the evolution equations can be performed by an exponential map:

$$\boldsymbol{F}_{\mathrm{p},n+1}^{-1} = e^{-\Delta t \boldsymbol{L}_{\mathrm{p}}} \boldsymbol{F}_{\mathrm{p},n}^{-1}, \tag{21}$$

that fulfils the requirement of plastic incompressibility exactly. Herein, n denotes the time step and Δt denotes the time step size. For further elaboration, the reader is referred to the articles by Sansour et al. [18,19].

3.3. Numerical setup and boundary conditions for the parameter identification process

In order to identify the material parameters of the described model, two experimental setups are used: the tension test and the torsion test. Both tests together provide a good basis for the parameter ID with relatively small effort because a variation in most of the material parameters can be measured directly in the experimentally observed reactions.

For both tests, the analysed samples are defined by their length in axial direction L_{x} and their diameter d. The general mesh setup is illustrated in Figure 3(a), with five parameters controlling the mesh refinement. The basis is the *Oh-structure* defined by the element boundaries in black. Refining the cross-section can be controlled by two parameters: the partitioning in circumferential direction n_{a}, indicated by the red lines, and the partitioning in radial direction n_{r}, which is indicated by the blue line. The refinement in axial direction is controlled by the parameter n_{x}, the order of the mapping functions describing the geometry by p_{g}, and the polynomial degree of the isotropic ansatz space for the trial and test functions of the 3D hexahedral solid elements is given by p_{A}. As a compact notation, they are summarised as $\mathscr{D}^{p_{\mathrm{A}}}_{n_{\mathrm{a}},\, n_{\mathrm{r}},\, n_{\mathrm{x}},\, p_{\mathrm{g}}}$.

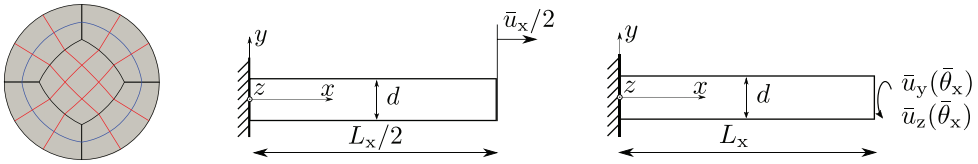

Figure 3. Setup of tension and torsion tests for parameter identification: (a) Oh-mesh $\mathscr{D}^{p_A}_{3,2,2,2}$, (b) setup tension, and (c) setup torsion.

3.3.1. Tension test. The boundary conditions and the geometrical parameters for the tension test can be seen in Figure 3(b). The sample is clamped on the left-hand side, while on the right-hand side, a displacement $\bar{u}_x$ is imposed and the displacements u_y and u_z are suppressed, $u_y = u_z = 0$. The symmetry in x-direction is exploited, as depicted in Figure 3(b).

The resulting forces and moments are computed at the boundary on the left-hand side ($x = 0$). Due to the simple load situation of the tension test, only the resulting force $\not{f}_x$ in x-direction at each load step i for a total of n_{ts} load steps is considered in the error computation:

$$e_{r,\,ten} = \sqrt{\frac{\sum_{i=1}^{n_{ts}} (\not{f}_{x,\,i} - \not{f}^{exp}_{x,\,i})^2}{\sum_{i=1}^{n_{ts}} (\not{f}^{exp}_{x,\,i})^2}} \cdot 100[\%], \tag{22}$$

using the experimental results $\not{f}^{exp}_{x,\,i}$.

3.3.2. Torsion test. The boundary conditions and geometrical parameters for the torsion test can be seen in Figure 3(c). The sample is clamped on the left-hand side, and on the right-hand side, a rotation is applied via the displacement components $\bar{u}_y$ and $\bar{u}_z$. Similar to the tension test, the resulting forces and moments are computed at the boundary on the left-hand side ($x = 0$). In this case, only the resulting moment $\mathscr{m}_x$ in x-direction at each load step i is considered in the error computation:

$$e_{r,\,tor} = \sqrt{\frac{\sum_{i=1}^{n_{ts}} (\mathscr{m}_{x,\,i} - \mathscr{m}^{exp}_{x,\,i})^2}{\sum_{i=1}^{n_{ts}} (\mathscr{m}^{exp}_{x,\,i})^2}} \cdot 100[\%], \tag{23}$$

where $\mathscr{m}^{exp}_{x,\,i}$ denotes the experimental measurements.

3.4. Convergence study for the parameter identification process

Due to the repeated computation of the finite element simulation during the ID process, an efficient choice has to be made for the spatial discretisation. A convergence study is carried out to ensure that the simulation is accurate while not using more degrees of freedom than necessary. It is useful to take a closer look at the *h*-refinement and *p*-refinement, which includes hierarchic trunk- and tensor-product ansatz spaces [20,21].

Figure 4 shows a plot of the relative root mean squared error as described in equations (22) and (23) of several refinements for the Oh-structure. The green curve shows tensor-product *p*-refinement ($i = p_g = p_A = 1, 2, ..., 5$) based on the finest mesh. Starting from the finest mesh using two different polynomial degrees ($\mathscr{D}^3_{3,2,4,3}$ marked by $+$, and $\mathscr{D}^5_{3,2,4,5}$ marked by *), the mesh is coarsened in each parameter n_a (blue), n_r (red), and n_x (black) separately. For the tension test in Figure 4(a), the coarsening of n_a (blue lines) and n_r (red lines) shows no relevant change in the accuracy, which leads to the conclusion

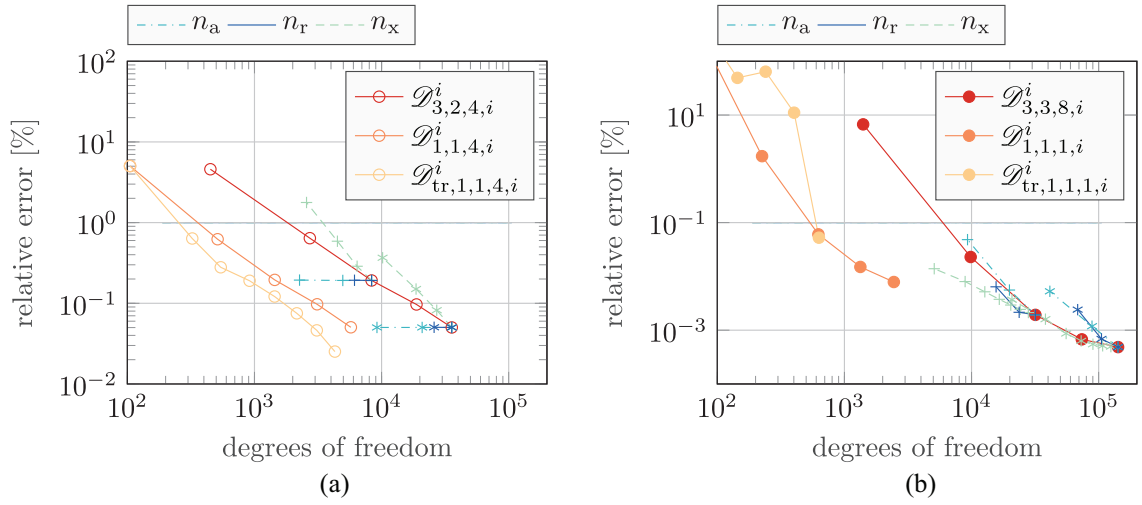

Figure 4. Convergence graphs for different refinements for tension and torsion: (a) tension test and (b) torsion test.

that n_a and n_r can be safely coarsened without a loss of accuracy. The coarsening in n_x (black lines), however, shows decreasing accuracy, which motivates keeping four elements along the axis. For comparison, the isotropic p-refinement using $n_a = 1$ and $n_r = 1$ and $n_x = 4$ is depicted in magenta, using the full tensor-product space, and in cyan, using the trunk ansatz space ($\mathscr{D}_{tr}$), both reducing the degrees of freedom significantly.

Remark. Only simple equidistant mesh partitioning is considered here, eventually introducing a small element at the boundary layer $x = 0$ could improve the results further.

In Figure 4(b), the convergence for the torsion test is plotted. Again, an isolated coarsening of each parameter n_a (blue), n_r (red), and n_x (black) is performed beginning at the finest mesh size for two polynomial degrees ($\mathscr{D}^3_{3,3,8,3}$ marked by $+$ and $\mathscr{D}^5_{3,3,8,5}$ marked by *). In contrast to the tension test, the parameters n_a and n_r are more relevant to the accuracy with more emphasis on n_a. The influence of n_x does not vanish, as it does with n_a and n_r for tension, but it has a less steep slope. The error for a minimal h-refinement and the tensor-product space, which already shows a good convergence, is plotted in magenta. The trunk ansatz space ($\mathscr{D}_{tr}$) for a similar h-refinement—plotted in cyan—shows a somewhat delayed convergence that starts to improve very fast as soon as face modes are included [20]. This behaviour for comparably low orders leads to the decision to use the tensor-product ansatz space.

The accuracy and reproducibility of the experimental results are expected to be at best around 1%, which gives a margin of accuracy that should be achieved by the FEM simulations. For simplicity, the same mesh is thus used for both tension and torsion, which requires a spatial discretisation with $\mathscr{D}^2_{2,1,4,2}$. This results in a relative error of 0.641% in the tension test and 0.122% error in the torsion test. Choosing different meshes for both simulations would result in a similar accuracy with fewer degrees of freedom—providing an even more efficient method.

3.5. Parameter identification: particle swarm method

The ID process is conducted using the particle swarm algorithm of the MATLAB optimisation toolbox, as it offers the possibility to define user-specific objective functions as well as pre-/post-processing functions. This allows for an easy handling to start an external FEM simulation and evaluate the results while providing the surrounding optimisation scheme. The particle swarm method is based on a set of n_p particles, each having an individual state $\boldsymbol{s}_i$, where i denotes the particle number. For each particle, the new state $\boldsymbol{s}'_i$ is then calculated by its current state $\boldsymbol{s}_i$ and a new increment $\boldsymbol{v}'_i$,

$$\boldsymbol{s}'_i = \boldsymbol{s}_i + \boldsymbol{v}'_i. \tag{24}$$

The increment is defined heuristically, and it introduces a social and a stochastic component by weighting the distance from the particles' current state to the best previous state $\boldsymbol{s}_i^*$ and the best state of the neighbourhood $\boldsymbol{s}_{\text{nbd}}^*$,

$$\boldsymbol{v}_i' = I\boldsymbol{v}_i + \boldsymbol{\phi_1} \circ (\boldsymbol{s}_i^* - \boldsymbol{s}_i) + \boldsymbol{\phi_2} \circ (\boldsymbol{s}_{\text{nbd}}^* - \boldsymbol{s}_i), \tag{25}$$

where I is an *inertia* like term, and $\boldsymbol{\phi_1}$ and $\boldsymbol{\phi_2}$ are the uniformly distributed random vectors. The operator $\circ$ in equation (25) represents the Hadamard product: $\boldsymbol{a} = \boldsymbol{b} \circ \boldsymbol{c} \Leftrightarrow a_j = b_j c_j$. The initial values of the states $\boldsymbol{s}_i$ and the initial increments $\boldsymbol{v}_i$ are chosen at random within a given range of admissible values. This allows for an efficient search that is not prone to settling in local minima—and it allows to exploit the usage of parallel computation as the FEM simulations for each particle can be performed in parallel. For a detailed description of the algorithm, the interested reader is referred to the MATLAB documentation [22] or the following articles [23–25].

In order to minimise the search space and thus reduce the number of material parameters, several assumptions are applied. First, the assumption of transverse isotropy is denoted by a new notation using the subscript f to denote a privileged or fibre direction and the subscript t to indicate the transverse directions. With respect to the prior notation, f replaces the direction 1, while t replaces directions 2 and 3—leading to the following simplifications for transversely isotropic materials in the hyperelastic part:

$$E_{\text{t}} = E_2 = E_3, \quad \nu_{\text{ft}} = \nu_{12} = \nu_{13}, \quad G_{\text{ft}} = G_{12} = G_{13}, \quad G_{\text{tt}} = G_{23} = \frac{E_2}{2(1+\nu_{23})}, \tag{26}$$

and the elasto-plastic part:

$$\sigma_{\text{f}} = {}^0\sigma_{11}, \quad \sigma_{\text{t}} = {}^0\sigma_{22} = {}^0\sigma_{33}, \quad \sigma_{\text{ft}} = {}^0\sigma_{12} = {}^0\sigma_{13}, \quad {}^0\sigma_{23} = \frac{{}^0\sigma_{22}}{\sqrt{3}}. \tag{27}$$

Second, Poisson's ratios ν_{ft} and ν_{tt} are not considered during the ID process, due to the lack of influence on the observed reactions with regard to the respective tension and torsion experiment. Thus, an assumption is made and referred to in the corresponding sections. Finally, the yield stress σ_{t} is set to be equal to σ_{f}, since it also has only marginal effects on the observed quantities. This leaves a total number of eight material parameters to be identified. The state s_i is defined by the remaining unknown material parameters used for the simulation $s_i = [E_{\text{f}}, E_{\text{t}}, G_{\text{ft}}, \sigma_{\text{f}}, \sigma_{\text{ft}}, \sigma_\infty, H, \delta]^{\text{T}}$.

For both simulations, the resulting force–displacement or moment–rotation curve is compared to the experimental data making use of the relative root mean squared error as mentioned in equations (22) and (23). The reaction force/moment of the simulation is computed at each load step for a given displacement/rotation. The measured reaction force/moment is interpolated through the closest data points of the experimental results. Since the torsion and tension tests should both be represented by the model with an equal quality, the objective function is defined by the relative error of both simulations,

$$e_{\text{r, ID}} = \frac{e_{\text{r, ten}} + e_{\text{r, tor}}}{2}. \tag{28}$$

4. Results of the experimental investigations and numerical simulations

4.1. PVC

Initially, a simple material (PVC) is investigated. It is expected that the PVC samples exhibit isotropic behaviour. This serves as a test for the experimental setup and also for the numerical ID process. Tensile and torsion tests served as a basis for the parameter ID, and a three-point bending was conducted to validate the identified parameters.

For the tension and torsion tests, the specimen's geometry and the mesh parameters for these geometries are listed in Table 1.

Table 1. Specimen geometry and mesh parameters for the simulations.

Experiment	L_x	d	n_a	n_r	n_x	p_g	p	n_{ts}	Maximum displacement/rotation
Tension	60 mm	10.45 mm	2	1	4	2	2	101	2 mm
Torsion	60 mm	10.45 mm	2	1	4	2	2	201	70°

Table 2. Lower and upper limits set for the parameter identification of polyvinyl chloride.

E_f	E_t	$\nu_{ft} = \nu_{tt}$	G_{ft}	$\sigma_f = \sigma_t$	σ_{ft}	$\Delta\sigma_\infty$	H	δ
2200 MPa	1800 MPa	0.41	850 MPa	18 MPa	12 MPa	3 MPa	1 MPa	30
3200 MPa	3200 MPa	0.41	1300 MPa	35 MPa	30 MPa	30 MPa	70 MPa	700

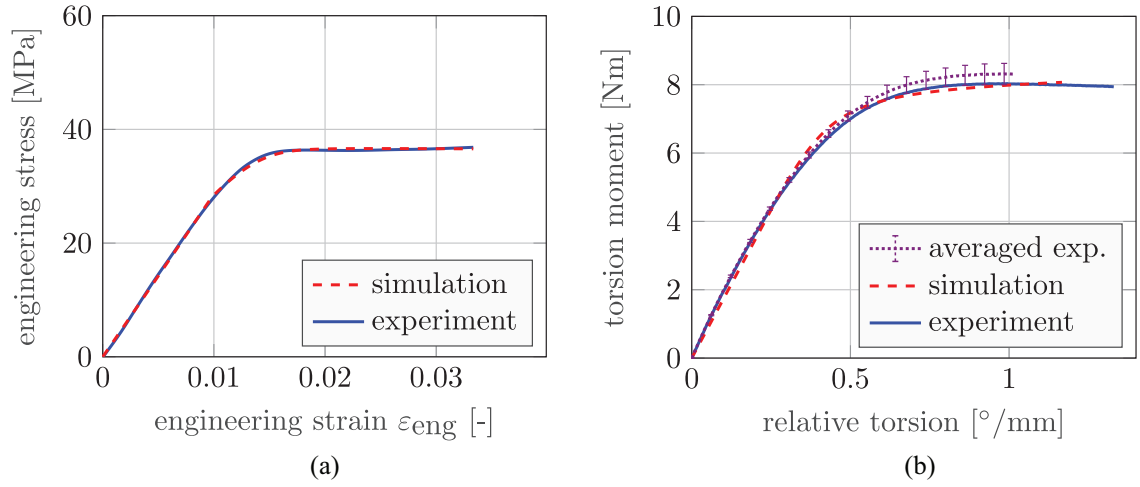

Figure 5. Comparison of the simulations with converged parameters to the experimental data for PVC: (a) tension test and (b) torsion test.

4.1.1. Identification of the parameters. For the parameter ID, upper and lower bounds were set based on an estimation of their possible range, see Table 2. Thereby, $E_f \approx \frac{\ell_x L_x}{\Delta l A_0} \approx \frac{\sigma_{eng}}{\varepsilon_{eng}}$ and $G_{ft} \approx \frac{m_x L_x}{\Delta\theta_x J_T}$ can be approximated for small deformations, where ℓ_x and m_x, as defined earlier, denote the force and the moment, respectively, A_0 represents the cross-section area, and J_T is the polar moment of inertia. As the elastic part of the experiments shows a good fit with these approximately calculated values, the range for these parameters can be set by allowing a small deviation of $\pm 15\%$ from the approximate value. A range for the yield stresses (σ_f, σ_t and σ_{ft}), can be determined by looking at the deformation path. The occurrence of a strongly non-linear deformation behaviour indicates plastic deformation as the strains are not large enough to explain this behaviour purely through hyperelasticity. Thus, the margins can be set safely before and after the estimated beginning of the elasto-plastic behaviour. The tension test is used for σ_f, and the torsion test is used for σ_{ft}. The corresponding shear stress during torsion can be computed by $\sigma_{ft} \approx m_x \frac{d/2}{J_T}$, while σ_f can be directly extracted from Figure 5(a). $\Delta\sigma_\infty$ denotes a variable used to ensure admissible combinations of the yield stress and the saturation stress (σ_∞), which is computed through $\sigma_\infty = \sigma_f + \Delta\sigma_\infty$. This guarantees a saturation stress larger than the yield stress, which would otherwise lead to undesired behaviour, see equation (16). When the non-linear hardening is saturated, only the linear hardening remains as a driving force—indicated by the flattening curve in the tension test and torsion test. While $\Delta\sigma_\infty$ describes the difference between yield stress and saturation, the exponential

Table 3. Identified parameters for PVC.

E_f	E_t	$\nu_{ft} = \nu_{tt}$	G_{ft}	$\sigma_f = \sigma_t$	σ_{ft}	$\Delta\sigma_\infty$	H	δ
2810 MPa	2538 MPa	0.41	850.1 MPa	28.41 MPa	20.26 MPa	8.81 MPa	31.84 MPa	648.2

PVC: polyvinyl chloride.

Table 4. Specimen geometry and mesh parameters for the simulation.

Experiment	L_x	d	r_s	r_p	p_g	p	n_{ts}	$\bar{u}_y$
Three-point bending	120 mm	10.45 mm	10 mm	1 mm	2	3	151	7.5 mm

hardening parameter δ is a measure for the speed of the saturation. Thus, an educated guess on the limits of $\Delta\sigma_\infty$ can be extracted from the experimental results, while δ remains within a broad range of possible values. Finally, the linear hardening H is the main driving force in the linear increase of the engineering stress or torsion moment after the saturation. Based on the steepness, the limits can be estimated with a larger range, as it is not as clear as other parameters. As mentioned in section 3.5 and noted in Table 2, the value for both Poisson's ratios is fixed to 0.41 [26]. Using the DIC results, Poisson's ratio was measured to be 0.37 based on the tensile strain and transverse strain. Together with the little influence on the reactions in the simulation, the deviation poses no loss of accuracy.

For the tensile test of PVC, the DIC method was used to determine the tensile strain of the sample. The strain is measured directly using the deformation at the centre of the sample instead of using the engineering strain based on the displacement of the clamps and the initial length. This leads to an adaptation of the boundary conditions to represent the *real* strain as closely as possible. Instead of a clamped boundary condition, the sample is fixed only in x-direction. This allows the cross-section to deform at both ends.

The particle swarm ID converges towards a solution with a remaining error of about $e_r \approx 1.48\%$, producing the set of material parameters listed in Table 3. Due to the stochastic nature of the optimisation process, there is no guarantee to find an optimal solution. In practice, however, the identified parameters vary only slightly around what seems to be an optimum for several runs. A large variance in the identified optimum usually hints towards an insufficiently covered search space or an ill-posed optimisation task.

The ID process is based on a swarm size of 40 particles and a maximum of 200 iterations. Due to sufficient convergence and only marginal improvements over the last 30 iterations, the ID process was stopped at iteration 77. Figure 5 illustrates the simulations of the force–displacement curve and the moment–rotation curve, respectively, with the final parameters and the experimental results used for ID. The simulations are depicted in red and show a good agreement with the corresponding experimental results (in blue) for both the tension test and the torsion test. Figure 5(b) shows an average of all torsion tests (plotted in violet) together with error bars of one standard deviation. The identified parameters in Table 3 do not yield perfectly isotropic parameters, but are slightly anisotropic, with a deviation of up to 20% from the isotropic theory in both the hyperelastic regime ($E_f \neq E_t$ and $G_{ft} \neq \frac{E_t}{2(1+\nu_{tt})}$) and the elasto-plastic regime ($\sigma_{ft} \neq \frac{\sigma_f}{\sqrt{3}}$). A possible explanation for a slight anisotropy can be found in the manufacturing process of the PVC rods—as it is often based on extrusion, which is why the polymer chains are aligned to some extent.

4.1.2. Validation of parameters. As a validation experiment for the identified material parameters, the three-point bending is chosen. The basic setup is presented in Figure 6(a) with the corresponding geometrical quantities listed in Table 4. A distance of 120 mm was kept between the two support points.

The symmetry is exploited using appropriate boundary conditions in the xy-plane at $z = 0$ and the yz-plane at $x = L_x/2$, thus computing only a quarter of the experiment. The punch on the right end and the bearing on the left side are both resolved by a quadrature point to surface contact method, as it is described in Bog et al. [27], and a local *hp*-refinement [28] serves to further improve the solution for the local contact areas, as can be seen in Figure 6(b).

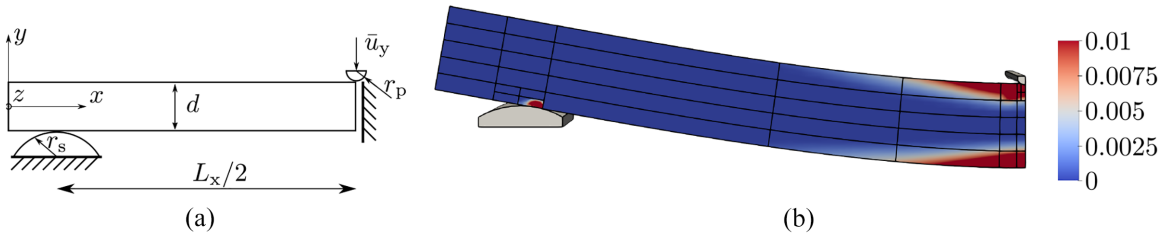

Figure 6. Setup and mesh at maximum deformation of three-point bending simulation for PVC experiment validation: (a) setup and (b) accumulated plastic strain.

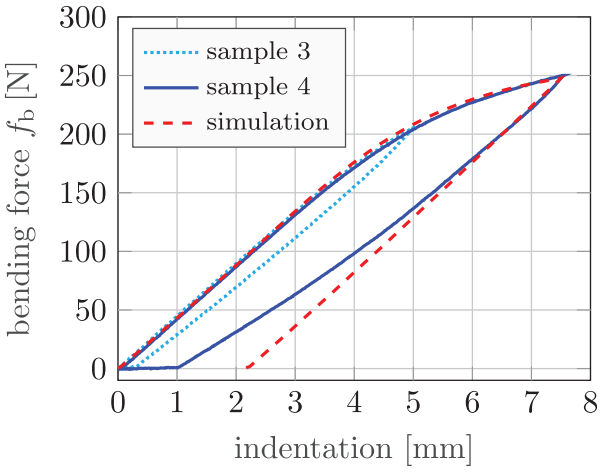

Figure 7. Three-point bending for the PVC sample with 120 mm length between the supports.

The results, plotted in Figure 7, show a good agreement with the experimental data for the loading path, which validates the identified material parameters. A slight offset can be identified at the unloading. The simulation predicts unloading in a linear purely elastic fashion, while the experimental data show a non-linear unloading that cannot be reproduced by the applied material model. This could be a result of viscoelastic effects, which are present in PVC but are not included in the applied material model.

4.2. CFRP

CFRP rods exhibit anisotropy, and they are much stiffer in the tensile direction compared to the transverse direction because of the orientation of the short carbon fibres along the longitudinal axis of the specimen. However, they have a homogeneous cross-section, and the relative movement between the carbon fibres and the embedding matrix is limited.

4.2.1. Identification of the parameters. Similar to the case of PVC, tensile and torsion experiments are used for parameter ID. The geometrical parameters for the specimens and the mesh used for the simulation are given in Table 5.

Due to the low stiffness and brittle nature of CFRP in the shear direction, the high pressure of the pneumatic clamps damages the CFRP rods, and low pressure leads to slipping between the clamps and the sample. In order to conduct the tensile and torsion experiments, the ends of the rods were thus cast in epoxy (cf. Figure 8). With the casting, the sample was clamped on the epoxy—not directly onto the surface of the CFRP rods.

The pneumatic clamps served to apply high pressure on the sample during the experiments, to ensure that no slip occurred. For the parameter ID, upper and lower bounds are defined based on an

Table 5. Specimen geometry and mesh parameters for the simulation.

Experiment	L_x	d	n_a	n_r	n_x	p_g	p	n_{ts}	Maximum displacement/rotation
Tension	90 mm	2 mm	1	1	4	3	3	201	2 mm
Torsion	50 mm	2 mm	1	1	4	3	3	201	60°

(a) (b)

Figure 8. (a) Cross-section of the CFRP rod with 2 mm diameter. (b) Epoxy casting around the CFRP rod for holding the specimen.

Table 6. Lower and upper limits set for the parameter identification of CFRP.

E_f	E_t	$\nu_{ft} = \nu_{tt}$	G_{ft}	$\sigma_f = \sigma_t$	σ_{ft}	$\Delta\sigma_\infty$	H	δ
90 GPa	5 GPa	0.3	2.6 GPa	250 MPa	7 MPa	200 MPa	1 GPa	3
110 GPa	30 GPa	0.3	3.4 GPa	600 MPa	30 MPa	700 MPa	4 GPa	1000

CFRP: carbon fibre-reinforced plastic.

Table 7. Best parameters identified for CFRP.

E_f	E_t	$\nu_{ft} = \nu_{tt}$	G_{ft}	$\sigma_f = \sigma_t$	σ_{ft}	$\Delta\sigma_\infty$	H	δ
110 GPa	5 GPa	0.3	2.98 GPa	250 MPa	21.6 MPa	647 MPa	4 GPa	445

CFRP: carbon fibre-reinforced plastic.

estimation of the possible range for the material parameters (see Table 6). The bounds are identified in a similar way as in the previous section 4.1 by analysing the tension and torsion experiments in Figure 9.

Poisson's ratio is set to $\nu_{ft} = 0.3$ drawing on values found in the literature [29]. As the influence on the reactions in the tension test and torsion test is too small, it is not possible to find a better value using the given data.

Again, $\Delta\sigma_\infty$ denotes a variable used to ensure admissible combinations of yield stress and the saturation stress, which is computed through $\sigma_\infty = \sigma_f + \Delta\sigma_\infty$. This guarantees a saturation stress larger than the yield stresses.

The best parameter set is given in Table 7, and the simulations with the identified parameters fit the experiments well, as shown in Figure 9(a) and (b). The blue curve represents the experiment used for the ID process. Additional experiments are averaged and plotted with one standard deviation in violet. A slight deviation from the original experiment can be observed, but the outcome is close and shows a similar qualitative path.

4.2.2. Validation of parameters. In order to validate the parameters, free bending with pre-torsion is considered. For the bending experiments, the specimen was mounted directly on the clamps without the epoxy

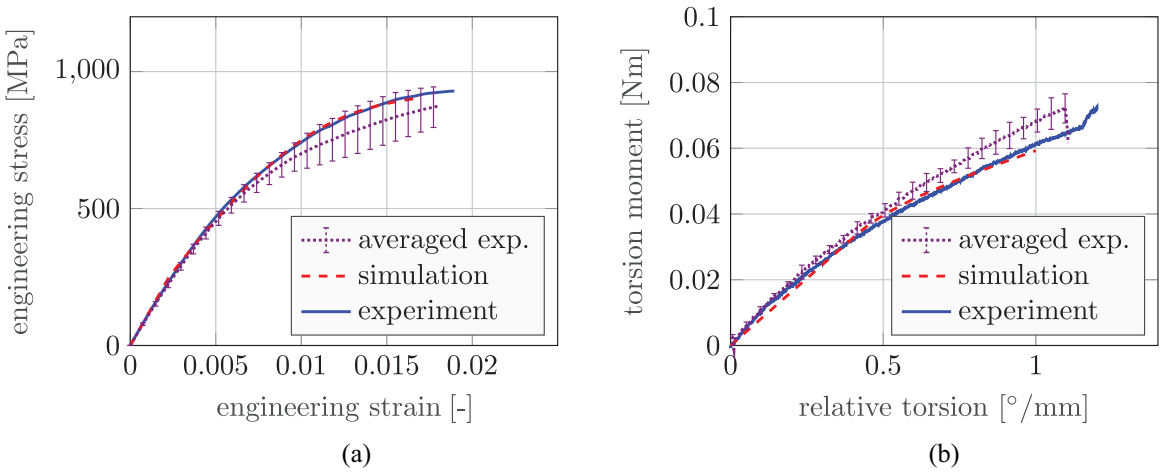

Figure 9. Fit of the parameter identification process for the tension and torsion experiment of CFRP: (a) tension test and (b) torsion test.

Table 8. Specimen geometry and mesh parameters for the free bending and free bending + torsion simulation for CFRP.

Experiment	L_x	d	n_a	n_r	n_x	p_g	p	n_{ts}	Maximum rotation
Free bending	100 mm	2 mm	2	1	8	3	3	121	30°
Torsion + free bending	80 mm	2 mm	2	1	8	3	3	81 + 40	40° torsion + 20° bending

CFRP: carbon fibre-reinforced plastic.

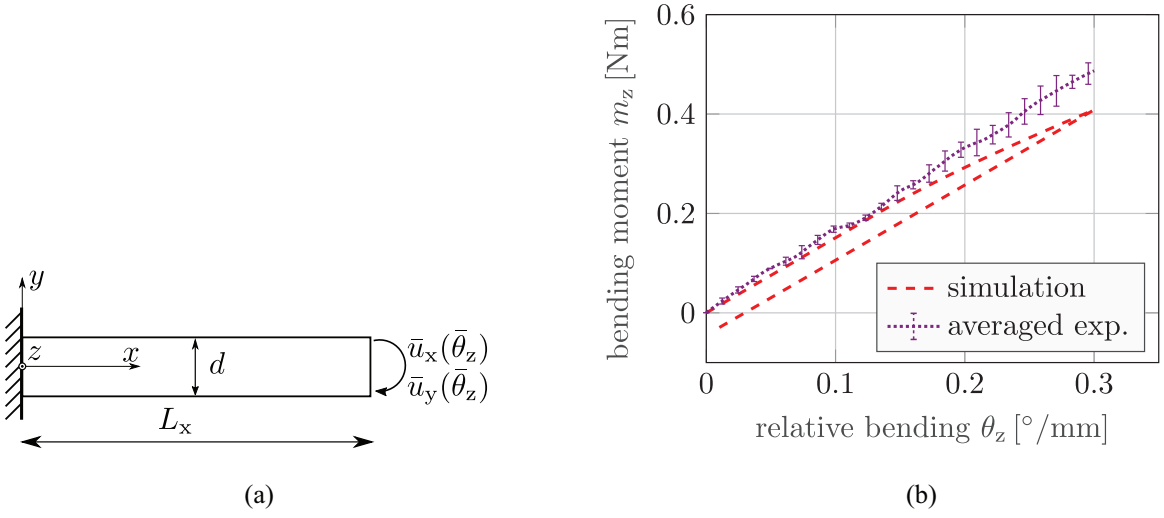

Figure 10. Boundary condition and results for free bending simulation and free bending experiments with the CFRP rod: (a) boundary conditions and (b) resulting bending moment.

casting, as the shear forces during these experiments are not too high. The geometry and the mesh parameters are given in Table 8.

Figure 10(b) shows that the bending moments computed in the simulation with the identified parameters lead to an approximate reproduction of the experimental results. The measured bending moment

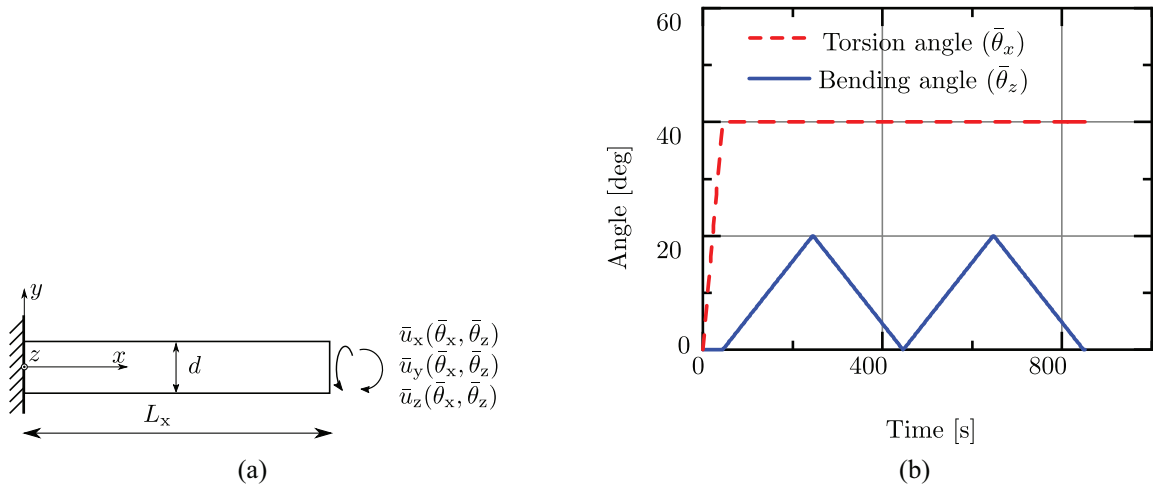

Figure 11. The boundary conditions for free bending with pre-torsion: (a) boundary conditions in the simulation and (b) prescribed torsional rotation $\bar{\theta}_x$ and bending angle $\bar{\theta}_z$.

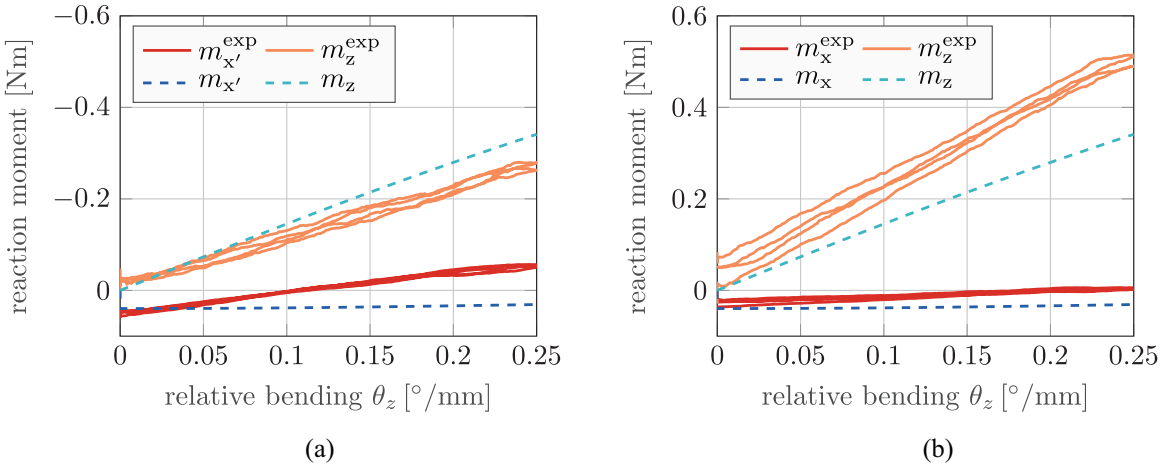

Figure 12. Resulting torsional moment m_x and bending moment m_z for both sides of the free bending simulation with pre-torsion of CFRP: (a) moving side (S89) and (b) fixed side (S90).

increases linearly with the increasing bending degree. Thus, an elastic behaviour is seen in the free bending experiment. The simulation shows a slight hysteresis, indicating that the yield stress is too low. This can be a result of the epoxy casting in the tension test, as the engineering strain is computed through the displacements of the clamps normalised by the initial length of the specimen. Thus, a deformation of the less stiff epoxy casting contributes to the tensile deformation as well.

To test the effect of the anisotropy and the coupling between the bending and torsion, a free bending experiment was conducted with a pre-torsion of 40° as shown in Figure 11. The bending and the torsion moments are measured at both ends of the CFRP rod. In the schematic representation of Figure 2(a), the left side rotates and the right side is fixed. The torsion motor is mounted on the right side. Sensor S89 measures the reaction forces on the left end and sensor S90 measures the reaction forces at the right end of the rod. Since the coordinate system of S89 rotates with respect to S90, the rotated coordinate system with its new directions is denoted by x' and y'.

The computed torsion and bending moments can be seen in Figure 12 and are—for both sides, S89 and S90—almost identical in their amplitude. The small difference is mainly a result of the rotated

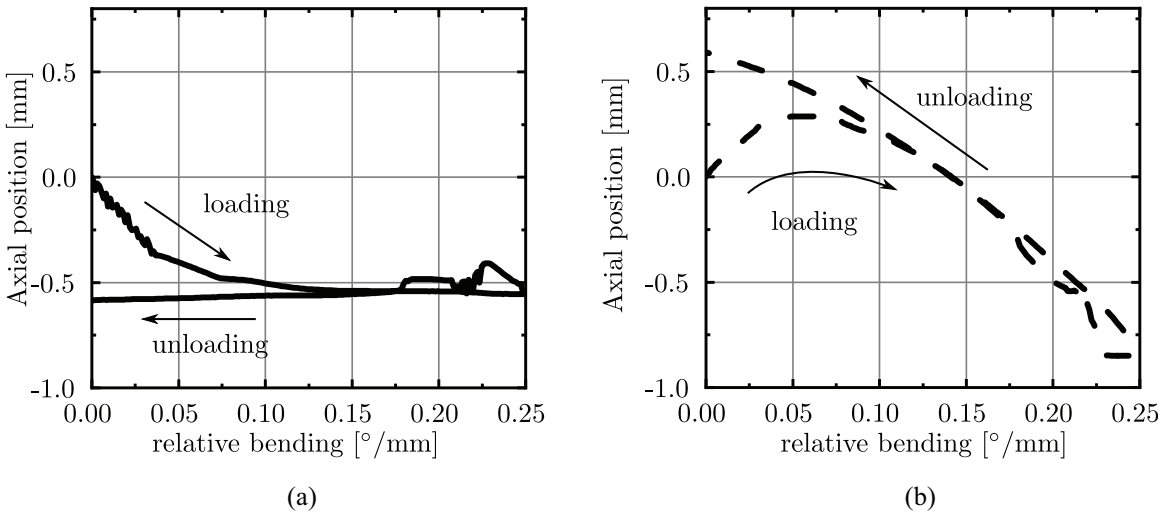

Figure 13. The change in the axial position of the ends during bending to compensate for the axial forces: (a) fixed side (S90) and (b) moving side (S89).

coordinate system in S89, as the resulting forces are nearly zero and have only a marginal influence, even with the given leverage arm.

In the experiments, however, an asymmetry is seen in the torsion and bending moment of both sides. This can be attributed to the movement of one of the ends to control the axial forces. In Figure 13, it can be seen that the rotating side moves to control the axial forces, whereas the fixed side stays stationary. The movement of the end along the axis of the rod changes the orientation of the carbon fibres with respect to the original position, which leads to a change in the torsion moment. Thus, a coupling between the tensile, bending, and torsion stiffness can be seen. The simulation results can reproduce the resulting torsion moment due to the pre-torsion and the bending moment with a slight deviation. The asymmetrical moments given in the experiment are not reproduced by the simulation as the boundary conditions deviate from the observed behaviour. This can be either addressed by changing the controlling algorithm or by adapting the boundary conditions to the observed displacements, which is currently work in progress.

4.3. Coaxial cable

The analysed coaxial cable consists of different layers along the cross-section—including the metallic wires, the dielectric insulation, the metallic sheath, and the polymer insulation. When subjected to deformation, these layers can move against each other, and thus influence the global material characteristics by introducing friction and a change of the original geometry. This results in a very complex material behaviour, which we seek to represent with an effective or macroscopic anisotropic material model as described in section 3.2. In accordance with the experiments on PVC and CFRP presented earlier, the ID is conducted using a tension and torsion test, while the validation is done using a free bending experiment.

4.3.1. Identification of the parameters. The geometrical parameters for tensile and torsion experiment are given in Table 9, while the boundary conditions are the same as described in the above ID processes.

The pre-defined limits for the material parameters are used to keep the ID process in a limited valid range of possible combinations. The limits are extracted from the experimental data in Figure 14 in a similar way as in section 4.1. They are listed in Table 10.

As it was not possible to find a meaningful Poisson's ratio in the literature for cables, the following is based on the same assumption as for PVC. Given that the effect on the reactions in tension and torsion is not sufficient to identify the parameter, it is not expected to have any relevant effect on the validation

Table 9. Specimen geometry for the experiments and the mesh parameters for the coaxial cable.

Experiment	L_x	d	n_a	n_r	n_x	p_g	p	n_{ts}	Maximum display/rotation
Tensile	90.5 mm	8.32 mm	2	1	4	2	2	101	2 mm
Torsion	90.54 mm	8.45 mm	2	1	4	2	2	201	80°

Table 10. Lower and upper limits set for the parameter identification of the coaxial cable.

E_f	E_t	$\nu_{ft} = \nu_{tt}$	G_{ft}	$\sigma_f = \sigma_t$	σ_{ft}	$\Delta\sigma_\infty$	H	δ
700 MPa	600 MPa	0.4	150 MPa	0.2 MPa	0.2 MPa	0.5 MPa	1 MPa	10
1000 MPa	1500 MPa	0.4	300 MPa	2 MPa	1 MPa	100 MPa	1000 MPa	1000

Table 11. Identified parameters for the coaxial cable.

E_f	E_t	$\nu_{ft} = \nu_{tt}$	G_{ft}	$\sigma_f = \sigma_t$	σ_{ft}	$\Delta\sigma_\infty$	H	δ
1000 MPa	600 MPa	0.4	194.2 MPa	0.784 MPa	1.0 MPa	0.716 MPa	65.31 MPa	893.6

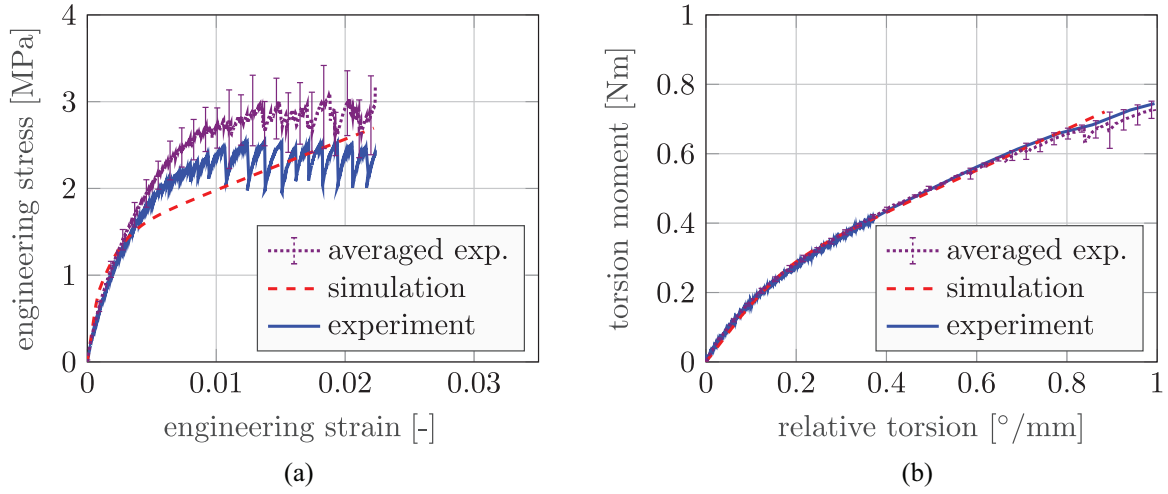

Figure 14. Comparison of the simulations with the experiments using the identified material parameters of the coaxial cable: (a) tension test and (b) torsion test.

experiments either. In Figure 14, the results for the ID process can be seen. The blue lines denote the experiments used for ID, while the red lines represent the simulation results for the parameters listed in Table 11. In addition, an average over all experiments is depicted (in violet) together with error bars of one standard deviation.

Both the torsion and tension simulation match the experiments well—with the difference that the tension experiment exhibits more oscillations. A discussion about the oscillations in the experiments is presented in the next section. In the tension test, in Figure 14(a), the slope in both the elastic and the inelastic part is different from the slope of the experiment. This is likely an effect of the large oscillations in the elasto-plastic regime, which interfere with an efficient minimisation of the error.

Table 12. Specimen geometry and mesh parameters for the free bending simulation of the coaxial cable.

L_x	d	n_a	n_r	n_x	p_g	p	n_{ts}	Maximum rotation
90 mm	8.3 mm	2	1	9	3	3	161	80°

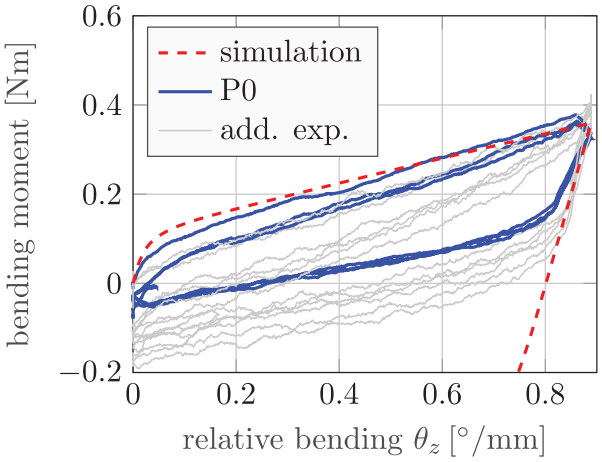

Figure 15. Free bending simulation and free bending experiments of the coaxial cable.

4.3.2. Free bending. The parameters identified from the tensile and torsion test are used to simulate the free bending experiment with the geometric parameters listed in Table 12.

The simulation results are plotted in Figure 15 in red together with the experimental results in blue or grey. Besides a slight difference in the slope, the curves fit well during the loading. This validates the material model together with the parameters identified earlier, and it shows that it is possible to use the anisotropic material model to represent the cable structure for tension, torsion, and free bending.

The unloading is similar to the experimental result in the elastic region but does not represent the inelastic region correctly. Considering that the chosen material model has no kinematic hardening term, it becomes clear that the observed behaviour cannot be represented. The experiment suggests that the elasto-plastic region is moved within the space and not only widened.

4.3.3. Discussion. The tensile experiments showed oscillations at larger strains, as shown in Figures 14(a) and 16. This is to be seen as a result of the interaction between the outer layers and the inner core of the cable. The outer layers deformed together with the inner core until the static friction between the layers was overcome and some of the layers started to slip, which repeats with further deformation. With a cable that is only clamped from the outer layer, the slipping is represented as a sudden drop in the measured stress. In order to confirm the hypothesis, the tensile experiment was conducted without the outer insulation layer. By removing the outer polymer layer, the force is directly carried by the metallic inner core of the cable. Thus, the deformation that is applied during the experiment directly deforms the metal which generates stresses that are an order higher than with the insulation as can be seen in Figure 16(b). The oscillation is also less as the slipping between the layers is reduced by removing one layer. This confirms the hypothesis that there is a slip between the outer sleeve and the inner structure.

This has severe implications on the measured data, as it is not desired to allow slipping of single layers, where the cable is clamped. Further research is therefore necessary to analyse the desired cable properties using a different type of clamping mechanism. It is also possible that this effect is also present in the free bending and torsion experiment—just not as clearly visible as in the tensile experiment.

The parameter ID process was nonetheless suitable to successfully identify the parameters for the given experiments of the coaxial cable, despite the stick–slip effect. The free bending experiment was able

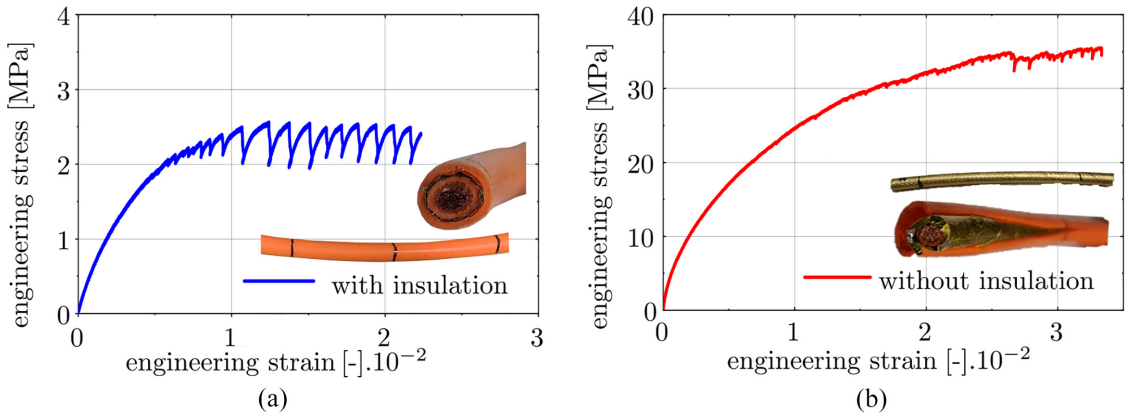

Figure 16. Tensile test (a) with the outer insulation layer and (b) without the outer insulation layer.

Table 13. Specimen geometry and mesh parameters for the free bending simulation with pre-torsion of the coaxial cable.

L_x	d	n_a	n_r	n_x	p_g	p	n_{ts}	Maximum rotation
90 mm	8.3 mm	2	1	9	3	3	180 + 161	90° torsion + 80° bending

to successfully validate the material parameters from the ID process. As the parameters were identified with the stick–slip effect, the reproduction of the free bending experiment with the identified parameters suggests that there is stick–slip in the free bending too. The effect is also evident in the difference between the first and the subsequent loading cycles. There is a larger dissipation in the first bending cycle than there is slip between the layers. With subsequent bending cycles, however, the slipping reduces and some layers stick together. This hypothesis can nevertheless only be answered by further experiments in which the movement between the layers is restricted across the cross-section. The rather large variance in the properties of plastic flow in Figure 14(a) is most likely also a result of the stick–slip effect—and this has to be taken into account when identifying the material properties.

4.3.4. Free bending and torsion. To test the effect of coupling between bending and torsion, free bending with a pre-torsion of 90° is considered. The geometry of the specimen and the mesh parameters are given in Table 13.

Similar to the CFRP rod, the reaction moments are measured at both ends of the cable. During the pre-torsion, the torsion moment in the experiment shows oscillation at higher degrees of rotations comparable to the oscillations observed in the tensile tests. This results in an over-prediction of the torsion moment in the simulation ($m_{x'}$) in Figure 17(a) and (b). However, the progression of the torsion moment during the bending of the cable is reproduced by the simulation with an offset. The coupling of the bending deformation with the torsion moment is evident in the experiment and is reproduced by the simulation results. The bending moment m_z in Figure 17(a) and (b) remains zero during the pre-torsion, and it increases on both sides of the sample in an elasto-plastic manner during bending. The bending moment is reproduced by the simulation and matches the experiment quite well. The identified parameters can thus reproduce the bending moment and the torsion moment for the coupled loading case. This once again highlights the asymmetrical progression of the bending moment, as the moving side (S89) and the fixed side (S90) are not the same in the experiments. This is due to the asymmetrical movement of the linear motor. During the bending, the axial forces are only controlled by the fixed side (S90), as shown in Figure 18, which causes the middle point of the sample to shift. The change in the position alters the bending moment recorded at the fixed side in the experiment. The simulation is able to reproduce the bending moment for the moving side (S89), and this bending moment is mirrored in the fixed side in the

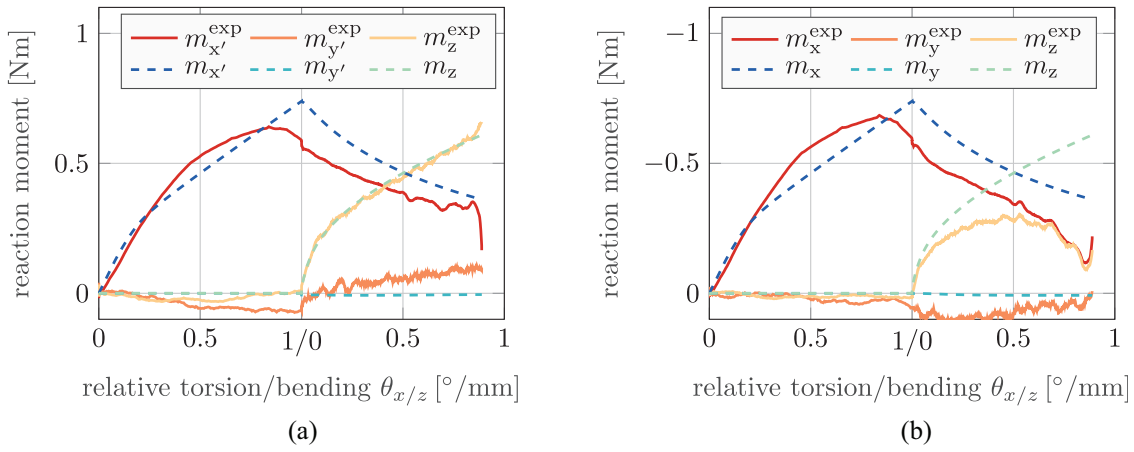

Figure 17. Reaction moments for both sides of the free bending simulation with pre-torsion of the coaxial cable: (a) moving side (S89) and (b) fixed side (S90).

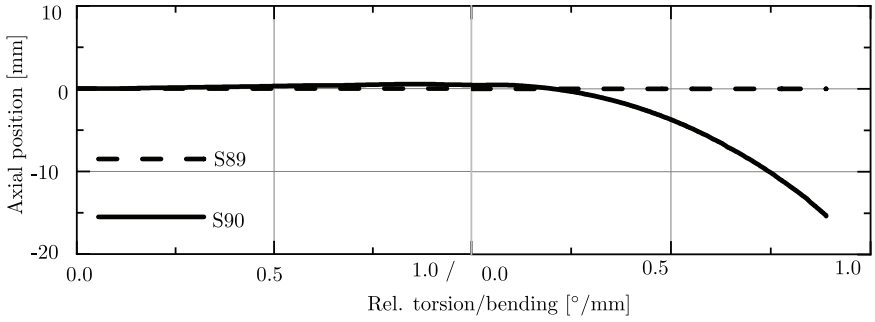

Figure 18. Axial forces are controlled by the movement of the fixed side only.

simulation. With the onset of the movement of the non-rotating side, the bending moment in the experiment starts to deviate from the simulation for the fixed side. As this violates the assumption of free bending in the simulation, the boundary conditions do not represent the experiment perfectly. The boundary conditions thus have to be altered to reproduce the movement in axial direction of the rotating end—or the controlling algorithm has to be changed to bring both, the experiment and the simulation, closer to each other.

5. Conclusion

Slender beam-like structures that represent rods and cables can be stretched, bent, or rotated during their application. These structures can be either isotropic or anisotropic materials on a macroscopic scale, and they have either homogeneous or inhomogeneous cross-sections. To characterise the anisotropic material, experiments must be conducted in all three loading directions. Due to the structural effects—such as movement of metallic wires inside a cable, or the orientation of fibres in a reinforced material—there is also a coupling in the materials' response with respect to the three loading cases.

In order to characterise such materials, an experimental setup was constructed to test different specimens with regard to tension, bending, torsion, and a coupling of bending and torsion. Three different material classes were characterised by experiments: PVC as an example for an isotropic homogeneous material, CFRP as an example for an anisotropic material with a homogeneous cross-section, and a coaxial cable representing an anisotropic material with as inhomogeneous cross-section. An anisotropic elasto-plastic material model was implemented in the FEM. The thin structures were discretised with the help of higher-order solid elements. The parameters identified with the experiments for tension and

torsion served as a basis for the simulation of the third load case: the bending. The parameters identified with the help of the particle swarm method revealed a good fit of the simulations with the experimental results for the different kinds of materials. However, due to the asymmetrical movement of the two linear motors during the free bending experiment, the moments on one side of the specimen were not the same as on the other side in the experiments. In contrast, the simulations assumed perfect symmetry of the boundary conditions and, therefore, led to identical values for the computed moments on both sides of the samples.

In the future, the linear motors for the free bending experiments will be controlled to enforce a symmetrical movement of the axial motors by modifying the control strategy. A penalty of the asymmetrical movement will be added on top of the zero axial force parameter. Moreover, the material with inhomogeneous cross-section will be discretised layer by layer to simulate the behaviour of the interaction/frictional dissipation between the layers, which could be of help in modelling the loading and unloading cases.

Funding

The author(s) disclosed receipt of the following financial support for the research, authorship, and/or publication of this article: The support of the DFG (Deutsche Forschungsgemeinschaft) under grant nos DU 405/14-1 and DI 430/43-1 is gratefully acknowledged.

ORCID iDs

André Hildebrandt https://orcid.org/0000-0001-9557-4549
Prateek Sharma https://orcid.org/0000-0001-6634-7881

References

[1] Dörlich, V, Linn, J, Scheffer, T, et al. Towards viscoplastic constitutive models for Cosserat rods. *Arch Mech Eng* 2016; 63(2): 215–230.
[2] Dörlich, V, Linn, J, and Diebels, S. Flexible beam-like structures—experimental investigation and modeling of cables. In: Altenbach, H, Jablonski, F, Müller, W, et al. (eds) *Advanced structured materials*, vol. 80. Cham: Springer Verlag, 2018, pp. 27–46.
[3] Foti, F, and Martinelli, L. Mechanical modeling of metallic strands subjected to tension, torsion and bending. *Int J Solids Struct* 2016; 91: 1–17.
[4] Rivlin, RS. Large elastic deformations of isotropic materials. I. Fundamental concepts. *Phil T R Soc London Ser A, Math Phys Sci* 1948; 240(822): 379–397.
[5] Johlitz, M, and Diebels, S. Characterisation of a polymer using biaxial tension tests. Part I: hyperelasticity. *Arch Appl Mech* 2011; 81(10): 1333–1349.
[6] Chen, Z, Scheffer, T, Seibert, H, et al. Macroindentation of a soft polymer: identification of hyperelasticity and validation by uni/biaxial tensile tests. *Mech Mater* 2013; 64: 111–127.
[7] Utting, WS, and Jones, N. Axial–torsional interactions and wire deformation in 19-wire spiral strand. *J Strain Anal Eng Des* 1988; 23(2): 79–86.
[8] Knapp, RH. Derivation of a new stiffness matrix for helically armoured cables considering tension and torsion. *Int J Num Meth Eng* 1979; 14(4): 515–529.
[9] Chu, TC, Ranson, WF, and Sutton, MA. Applications of digital-image-correlation techniques to experimental mechanics. *Exp Mech* 1985; 25: 232–244.
[10] Heißerer, U, Hartmann, S, Düster, A, et al. On volumetric locking-free behavior of p-version finite elements under finite deformations. *Commun Numer Meth Eng* 2008; 24(11): 1019–1032.
[11] Netz, T, Düster, A, and Hartmann, S. High-order finite elements compared to low-order mixed element formulations. *ZAMM-Z Angew Math Mech* 2013; 93(2-3): 163–176.
[12] Dörlich, V. *Experimentelle Untersuchung und konstitutive Modellierung des inelastischen Verhaltens von Kabeln*. PhD Thesis, Saarland University, Saarbrücken, 2020.
[13] Giorgio, I. A discrete formulation of Kirchhoff rods in large-motion dynamics. *Math Mech Solids* 2020; 25(5): 1081–1100.
[14] Harsch, J, Capobianco, G, and Eugster, SR. Finite element formulations for constrained spatial nonlinear beam theories. *Math Mech Solids* 2021; 26(12): 1838–1863.
[15] Kröner, E. Allgemeine Kontinuumstheorie der Versetzungen und Eigenspannungen. *Arch Ration Mech Anal* 1959; 4: 273–334.

[16] Besseling, JF. A thermodynamic approach to rheology. In: Parkus, H, and Sedov, LI (eds) *Irreversible aspects of continuum mechanics and transfer of physical characteristics in moving fluids*. Vienna: Springer, 1968, pp. 16–53.
[17] Lee, EH. Elastic-plastic deformation at finite strains. *J Appl Mech* 1969; 36(1): 1–6.
[18] Sansour, C, Karšaj, I, and Sorić, J. A formulation of anisotropic continuum elastoplasticity at finite strains. Part I: modelling. *Int J Plasticity* 2006; 22(12): 2346–2365.
[19] Sansour, C, Karšaj, I, and Soric, C J. On a numerical implementation of a formulation of anisotropic continuum elastoplasticity at finite strains. *J Comput Phys* 2008; 227(16): 7643–7663.
[20] Düster, A, Bröker, H, and Rank, E. The p-version of the finite element method for three-dimensional curved thin walled structures. *Int J Numer Meth Eng* 2001; 52: 673–703.
[21] Szabó, B, and Babuška, I. *Finite element analysis*. Chichester: John Wiley & Sons, 1991.
[22] Matlab documentation. Particle swarm optimization algorithm, https://www.mathworks.com/help/gads/particle-swarm-optimization-algorithm.html (accessed 26 January 2022).
[23] Eberhart, R, and Kennedy, J. Particle swarm optimization. In: *Proceedings of the IEEE international conference on neural networks*, vol. 4, Perth, WA, Australia, 27 November–1 December 1995, pp. 1942–1948. New York: IEEE.
[24] Mezura-Montes, E, and Coello, CAC. Constraint-handling in nature-inspired numerical optimization: past, present and future. *Swarm Evol Comput* 2011; 1(4): 173–194.
[25] Pedersen, MEH. *Good parameters for particle swarm optimization* (Tech Rep HL1001). Copenhagen: Hvass Lab, 2010, pp. 1551–3203.
[26] polymerdatabase. Typical Poisson's ratios of polymers at room temperature, http://polymerdatabase.com/polymer%20physics/Poisson%20Table.html (accessed 31 January 2022).
[27] Bog, T, Zander, N, Kollmannsberger, S, et al. Weak imposition of frictionless contact constraints on automatically recovered high-order, embedded interfaces using the finite cell method. *Comput Mech* 2018; 61(4): 385–407.
[28] Zander, N, Bog, T, Kollmannsberger, S, et al. Multi-level hp-adaptivity: high-order mesh adaptivity without the difficulties of constraining hanging nodes. *Comput Mech* 2015; 55(3): 499–517.
[29] Al-Mayah, A, Soudki, K, and Plumtree, A. Mechanical behavior of CFRP rod anchors under tensile loading. *J Compos Construct* 2001; 5(2): 128–135.

Appendix 1

Material parameters of orthotropic elasto-plasticity

The hyperelastic material parameters can be set up using Young's moduli E_i, Poisson's ratios ν_{ij}, and shear moduli G_{ij} for all three directions.

Table 14. Hyperelastic material parameters.

$\alpha_1 = -\alpha_4 - \alpha_7 - \alpha_8 - 2\alpha_{10}$	$\alpha_7 = E_2 \frac{\nu_{12}+\nu_{13}\nu_{32}}{4m}$
$\alpha_2 = -\alpha_5 - \alpha_7 - \alpha_9 - 2\alpha_{11}$	$\alpha_8 = E_3 \frac{\nu_{13}+\nu_{12}\nu_{23}}{4m}$
$\alpha_3 = -\alpha_6 - \alpha_8 - \alpha_9 - 2\alpha_{12}$	$\alpha_9 = E_3 \frac{\nu_{23}+\nu_{13}\nu_{21}}{4m}$
$\alpha_4 = \frac{1}{4}\left(\frac{1-\nu_{23}\nu_{32}}{m} E_1 - 8\alpha_{10}\right)$	$\alpha_{10} = \frac{1}{8}(G_{12}+G_{13}-G_{23})$
$\alpha_5 = \frac{1}{4}\left(\frac{1-\nu_{13}\nu_{31}}{m} E_2 - 8\alpha_{11}\right)$	$\alpha_{11} = \frac{1}{8}(G_{12}-G_{13}+G_{23})$
$\alpha_6 = \frac{1}{4}\left(\frac{1-\nu_{12}\nu_{21}}{m} E_3 - 8\alpha_{12}\right)$	$\alpha_{12} = \frac{1}{8}(-G_{12}+G_{13}+G_{23})$

The abbreviation m is defined by:

$$m = 1 - \nu_{12}\nu_{21} - \nu_{23}\nu_{32} - \nu_{13}\nu_{31} - 2\nu_{12}\nu_{23}\nu_{31}. \tag{29}$$

and Poisson's ratios ν_{ij} are related to their counterpart ν_{ji} through:

$$\frac{\nu_{ij}}{E_i} = \frac{\nu_{ji}}{E_j}, \tag{30}$$

see Sansour et al. [18].

Table 15. Elasto-plastic material parameters.

$\beta_1 = \frac{1}{{}^0\sigma_{11}^2} - \beta_7$	$\beta_4 = -\left(\frac{1}{{}^0\sigma_{11}^2} + \frac{1}{{}^0\sigma_{22}^2} - \frac{1}{{}^0\sigma_{33}^2}\right)$	$\beta_7 = \frac{1}{2}\left(\frac{1}{{}^0\sigma_{12}^2} + \frac{1}{{}^0\sigma_{13}^2} - \frac{1}{{}^0\sigma_{23}^2}\right)$
$\beta_2 = \frac{1}{{}^0\sigma_{22}^2} - \beta_8$	$\beta_5 = -\left(\frac{1}{{}^0\sigma_{11}^2} - \frac{1}{{}^0\sigma_{22}^2} + \frac{1}{{}^0\sigma_{33}^2}\right)$	$\beta_8 = \frac{1}{2}\left(\frac{1}{{}^0\sigma_{12}^2} - \frac{1}{{}^0\sigma_{13}^2} + \frac{1}{{}^0\sigma_{23}^2}\right)$
$\beta_3 = \frac{1}{{}^0\sigma_{33}^2} - \beta_9$	$\beta_6 = -\left(-\frac{1}{{}^0\sigma_{11}^2} + \frac{1}{{}^0\sigma_{22}^2} + \frac{1}{{}^0\sigma_{33}^2}\right)$	$\beta_9 = \frac{1}{2}\left(-\frac{1}{{}^0\sigma_{12}^2} + \frac{1}{{}^0\sigma_{13}^2} + \frac{1}{{}^0\sigma_{23}^2}\right)$

In order to define an orthotropic yield function for the elasto-plasticity, the individual yield stresses ${}^0\sigma_{ij}$ are used to define a certain limit load for each of the six independent stress components. They can be reformulated in nine parameters β_i used in the definition in Table 15, where ${}^0\sigma_{ij} = {}^0\sigma_{ji}$ for $i \neq j$ corresponds to the stress states of pure shear and ${}^0\sigma_{ji}$ for $i = j$ are the uniaxial yield stresses [19].